Journal of Modern Optics
Vol. 58, Nos. 5–6, 10–20 March 2011, 365–383

Taylor & Francis
Taylor & Francis Group

The photonic Wannier function approach to photonic crystal simulations: status and perspectives

Kurt Busch*, Christian Blum, Alexandra M. Graham, Daniel Hermann, Martin Köhl, Patrick Mack and Christian Wolff

Institut für Theoretische Festkörperphysik and DFG-Center for Functional Nanostructures (CFN), Karlsruhe Institute of Technology (KIT), Wolfgang-Gaede-Str. 1, 76131 Karlsruhe, Germany

(*Received 16 August 2010; final version received 20 September 2010*)

Photonic crystals represent a novel platform for the realization of integrated photonic circuits with numerous applications. This article reviews the present status of a computational approach dedicated to these systems that is based on photonic Wannier functions. The workings of the Wannier function approach are illustrated by way of selected examples. In addition, we discuss the advantages and limitations of this approach and sketch potential future developments.

Keywords: photonic Wannier functions; photonic crystals; numerical simulation

1. Introduction

Over the past two decades, photonic crystals (PhCs), i.e. periodic arrays of dielectric materials, have developed from a theoretical concept [1,2] to a mainstream research activity that spans from fundamental research [3,4] all the way to applied areas such as telecommunication [5] and sensing [6]. With this increased maturity and importance comes a corresponding increased demand for accurate PhC computations, both regarding the design of PhC structures (or entire functional elements, devices, or systems) and the interpretation of measurements. Here, the very nature of PhCs implies numerically large problems, even for simple PhC systems. The defining feature of a PhC is its photonic band structure, i.e. a multi-branch dispersion relation with frequency regions of extremely slow group velocities, forbidden frequency ranges for certain directions (the so-called stop bands), and even frequency ranges where propagation is forbidden irrespective of direction (the so-called photonic band gaps [PBGs]). In particular, PBGs may be exploited by deliberately introducing deviations from periodicity in order to realize cavities, waveguiding structures, and entire integrated optical circuits. In such circuitry, radiation of certain frequencies remains localized in the vicinity of the 'intentional defects' and is protected against leakage by the PBG effect [3]. This band structure is the result of the interplay of strong scattering from the individual units (Mie scattering) that make up the PhC array and the Bragg scattering associated with the array itself. As the lowest Bragg order corresponds to a periodicity of about half a wavelength, any reasonable PhC functional element comprises several unit cells, each of which features an internal (sub-wavelength) structure that needs to be resolved by the simulation tool. As a rule of thumb, all-purpose solvers such as those based on finite-difference of finite-element approaches require at least 20 degrees of freedom per wavelength and spatial dimension in order to arrive at a satisfactory spatial resolution. As a result, computations of two-dimensional (2D) and three-dimensional (3D) PhC structures and functional elements quickly require considerable computational resources.

On the other hand, 'just' computing the photonic band structure (along with the corresponding eigenmodes, commonly referred to as Bloch functions) is – by virtue of the Bloch–Floquet theorem – a relatively straightforward task [3]. In view of the fact that most of the above-mentioned functional elements (or 'intentional defects') in some sense represent a perturbation of an otherwise ideal PhC structure, one is tempted to construct a dedicated Bloch-function-based computational tool. Unfortunately, Bloch functions are modulated plane waves and are, therefore, ill-suited for representing localized optical fields. At this point, concepts originally developed in electronic structure theory come to the rescue. More precisely, Wannier

*Corresponding author. Email: kurt.busch@kit.edu

ISSN 0950–0340 print/ISSN 1362–3044 online

DOI: 10.1080/09500340.2010.526256
http://www.informaworld.com

functions (WFs) can be constructed from Bloch functions by virtue of certain unitary transformations that, essentially, correspond to lattice Fourier transforms. As a consequence, the set of WFs represents a complete set of basis functions that contains the full information about the photonic band structure of the underlying PhC. That WFs could be utilized for computing PhC structures has been recognized early on [7] but the actual generation of WFs remained problematic. This is partly related to the fact that the well known semi-analytical tight-binding method of solid-state theory has had only limited success in the case of PhCs – even to date only the simplest case of E-polarized light in 2D PhCs that consist of high-index posts could be addressed within such an approach [8,9]. Constructing WFs directly from numerically obtained Bloch functions is a much harder task and, again, advances in electronic structure theory [10] have opened the door for progress in the construction [11–13] and the usage [11,13–19] of WFs in PhC simulations.

With this work, we aim at providing a (necessarily somewhat biased) review regarding the present state of WF-based computation techniques for PhC structures along with a discussion of promising avenues for future developments. In Section 2, we provide a basic introduction into the properties and usage of Wannier functions in the framework of simple one-dimensional (1D) systems. This is followed by an exposition in Section 3 of the current state-of-the-art of Wannier-function based simulation techniques for 2D PhCs structures both regarding E- and H-polarized radiation. Finally, in Section 4 we describe recent developments regarding the simulation of 3D PhCs and the construction of Green's function approaches via WFs. This naturally leads to a discussion of future directions of WF-based PhC simulations.

2. 1D systems: basic properties and usage of Wannier functions

One-dimensional PhCs, i.e. periodically layered dielectric media, were well studied long before the notion of photonic crystals had been coined. They represent interesting physical systems in their own right with numerous applications [20]. For these systems, WFs have not been used extensively but a recent work [21] indicates that the multi-resolution properties of WFs will also be useful for the analysis of 1D PhC structures. On the other hand, 1D systems allow for analytical statements regarding the localization properties of WFs [22,23] and certain intentional defect structures [24]. In turn, this allows for extensive performance studies of the WF method in general and specific implementations of the method in particular.

We start our analysis by noting that in a linear system and for propagation normal to the stacking direction of the layers, the system can be described by two equivalent (but not identical) approaches that are based on either the transverse electric or the transverse magnetic field, $E(x)$ and $H(x)$,

$$\partial_x^2 E(x) + \frac{\omega^2}{c^2}\,\epsilon(x)\,E(x) = S^{(E)}(x) \quad \text{or}$$
$$\partial_x\left(\frac{1}{\epsilon(x)}\,\partial_x H(x)\right) + \frac{\omega^2}{c^2} H(x) = S^{(H)}(x). \qquad (1)$$

Here, ∂_x denotes the derivative with respect to x and we have assumed linearly polarized fields. The distribution of the dielectric material is described by a spatially varying dielectric constant $\epsilon(x)$ such that the x-axis represents the stacking direction. In the optical regime we can safely assume that the magnetic permeability μ equals one. As usual, the wave equations (1) above have been derived from Maxwell's curl-equations and we would like to note that in both cases Maxwell's divergence-equations are automatically satisfied, too. Furthermore, $S^{(E/H)}(x)$ represents a source term for the electric (superscript (E)) or magnetic (superscript (H)) field.

The seemingly innocuous statement about the equivalence of the two approaches acquires more weight once we note that at material interfaces the boundary conditions for $E(x)$ and $H(x)$ are quite different: while $E(x)$ exhibits a continuous first derivative across a material interface located at x_0, the derivative of $H(x)$ exhibits a discontinuity that is given by the dielectric contrast, i.e. $\partial_x H(x_0+0_+)/\epsilon(x_0+0_+) = \partial_x H(x_0-0_+)/\epsilon(x_0-0_+)$. Here, 0_+ denotes an infinitesimally small positive number. As we will discuss below, these properties of the fields at material interfaces strongly influence the convergence characteristics of the different WF-approaches. For an ideal 1D PhC (lattice period a) with lattice-periodic dielectric profile $\epsilon_p(x) = \epsilon_p(x+a)$, equations (1) admit solutions in the form of Bloch functions, $E_{nk}(x) = \exp(ikx) f_{nk}(x)$ or $H_{nk}(x) = \exp(ikx)\, g_{nk}(x)$. Here, n and k denote band index and 1D wave 'vector', respectively, where the latter lies in the first Brillouin zone (BZ). In addition, $f_{nk}(x) = f_{nk}(x+a)$ and $g_{nk}(x) = g_{nk}(x+a)$ represent lattice periodic functions [3].

These spatially extended Bloch functions may now be processed into spatially localized WFs for the electric or magnetic field (superscript (E) or

(H)) by virtue of a generalized lattice Fourier transform

$$W_{nR}^{(E)}(x) = \sum_{n'} \int_{\mathrm{BZ}} \mathrm{d}k\, e^{-ikR}\, U_{nn'}^{(E)}(k)\, E_{n'k}(x),$$
$$W_{nR}^{(H)}(x) = \sum_{n'} \int_{\mathrm{BZ}} \mathrm{d}k\, e^{-ikR}\, U_{nn'}^{(H)}(k)\, H_{n'k}(x). \quad (2)$$

Here, $R \in \mathcal{R} \equiv \{la;\, l \text{ integer}\}$ denotes an arbitrary 1D lattice 'vector' and $U_{nn'}^{(E/H)}(k)$ represents a unitary-matrix-valued function of the wave 'vector' k that, for a given k-value, describes a unitary transformation between the bands. In practice, the k-integration in Equation (2) is carried out by discretizing the BZ with a finite number of k-points. The resulting WFs are labelled by the (generalized) band index n and the 1D lattice 'vector' R associated with the unit cell around which the WF is localized.

The set of all Wannier functions constitutes a complete orthonormal set of localized basis functions, which contains the full information about the photonic band structure of the underlying PhC. The corresponding orthonormality relations depend on the choice of whether the electric or magnetic field formulation is used. Explicitly, we have

$$\langle W_{nR}^{(E)} | \epsilon_{\mathrm{p}}(x) | W_{n'R'}^{(E)} \rangle = \delta_{nn'}\, \delta_{RR'} = \langle W_{nR}^{(H)} | W_{n'R'}^{(H)} \rangle \quad (3)$$

for all bands n, n' and all lattice 'vectors' $R, R' \in \mathcal{R}$. In the above expressions, we have introduced compact notations $\langle f | g \rangle = \int \mathrm{d}x f^*(x)\, g(x)$ and $\langle f | \epsilon_{\mathrm{p}}(x) | g \rangle = \int \mathrm{d}x f^*(x)\, \epsilon_{\mathrm{p}}(x)\, g(x)$ for two arbitrary complex-valued functions $f(x)$ and $g(x)$. In both cases, the integration is over the entire space. Finally, δ_{ij} denotes the Kronecker symbol for the (discrete) indices i and j.

In addition, the Wannier functions inherit certain translational properties from the Bloch functions that are particularly useful for numerical purposes

$$W_{nR}^{(E/H)}(x) = W_{n0}^{(E/H)}(x - R) \quad \forall R \in \mathcal{R}. \quad (4)$$

As a result, only the Wannier functions that belong to the PhC unit cell which contains the origin (labeled by the lattice 'vector' 0) have to be constructed explicitly. Furthermore, since the WFs are constructed as a superposition of Bloch functions, which themselves are solutions to the 1D wave equations (1), these 1D WFs also inherit the corresponding properties of continuous (electric field WF) or discontinuous (magnetic field WF) first derivatives at material interfaces as discussed above.

In general, the set $\{U_{nn'}^{(E/H)}(k);\, k \in \mathrm{BZ}\}$ of all unitary transformations between the bands has to be determined numerically – analytical results are available only for special cases [10,22,23]. Perhaps the most natural way to proceed is to consider the spread functional

$$\Omega^{(E/H)}\left[\left\{U_{nn'}^{(E/H)}(k)\right\}\right] = \sum_{n} \left(\left\langle W_{n0}^{(E/H)} | x^2 | W_{n0}^{(E/H)} \right\rangle - \left(\left\langle W_{n0}^{(E/H)} | x | W_{n0}^{(E/H)} \right\rangle \right)^2 \right), \quad (5)$$

as a measure of the localization of the WFs and to minimize this functional with respect to the free parameters associated with the unitary transformations. In practice, for a given number of k-points in the numerical integration of Equation (2) and a finite group of bands n for which the spread functional should be minimized, this yields a large but finite nonlinear minimization problem. In essence, these unitary transformations address the fact that (i) the Bloch functions are determined only up to a global (but possibly band- and k-dependent) phase, (ii) band degeneracies and (in 2D and 3D) band crossings may occur, and (iii) avoided crossings occur where the Bloch functions on either side of the crossing continuously exchange their symmetry properties as the wave vector varies through the avoided crossings. It is, therefore, plausible that the minimization of the spread functional, Equation (5), leads to a continuously varying global phase of the Bloch functions and allows for a relabeling of the Bloch functions as well as a demixing of the Bloch functions' symmetries such that maximally localized WFs are obtained [10]. In the case of 1D systems, individual bands are energetically isolated from each other so that the original algorithm of Marzari and Vanderbilt [10] can be directly employed. We find that when the Bloch functions at the center of the BZ, i.e. at the Γ-point, are truncated to the Wigner–Seitz cell centered at the origin, we obtain excellent trial functions for projecting the raw Bloch functions for all remaining wave 'vectors' as required in the preprocessing step of the algorithm. For the actual minimization of the spread function, Equation (5), we use a standard conjugate gradient scheme.

In Figure 1, we display the maximally localized electric and magnetic field WFs associated with bands 1, 2, 3, and 48 for a 1D PhC that consists of equally sized layers of silicon ($\epsilon_{\mathrm{Si}} = w12$) and air ($\epsilon_{\mathrm{Air}} = 1$). These WFs have been constructed for each band separately by using a total of 99 k-points. The corresponding Bloch functions have been computed via the MPB band structure package [25] with a spatial resolution of 512 points within the PhC's unit cell. The different behaviour of the electric and magnetic WFs at material interfaces is clearly visible. In addition, the

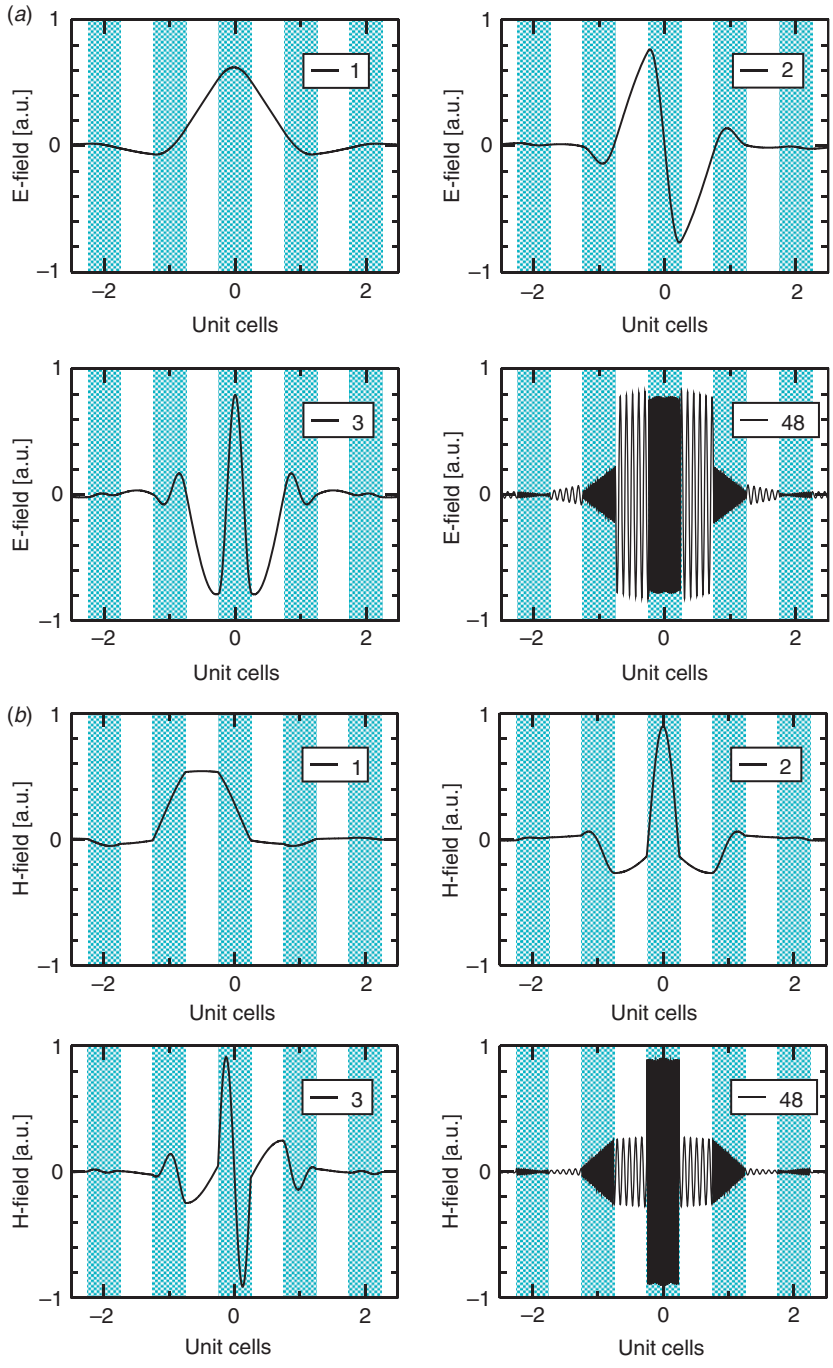

Figure 1. Electric (*a*) and magnetic (*b*) Wannier functions for bands 1, 2, 3, and 48 of a 1D PhC that consists of equally sized layers of silicon and air. The shaded areas correspond to the silicon layers. The underlying photonic band structure of this system is depicted in Figure 2(*b*). Note the different behavior of electric and magnetic WFs at material interfaces. (The color version of this figure is included in the online version of the journal.)

WFs in Figure 1 exhibit excellent localization and symmetry properties that reflect the symmetry of the underlying lattice [22]. More precisely, we find that within the limit set by the numerical discretization both electric and magnetic WFs follow the analytically predicted localization properties $W_{n0}^{(\mathrm{E/H})}(x) \propto x^{-3/4} \times \exp(-h_n x)$, where the localization length h_n for the WF associated with band n is proportional to the distance of the branch point of the photonic band structure's analytical continuation into the complex k-plane (see [23]). In simple cases, the minimal energetic separation of band n to bands $n-1$ and $n+1$ for real values of k provides an estimate of this distance h_n. We illustrate this in Figure 2, where we display the magnetic WFs

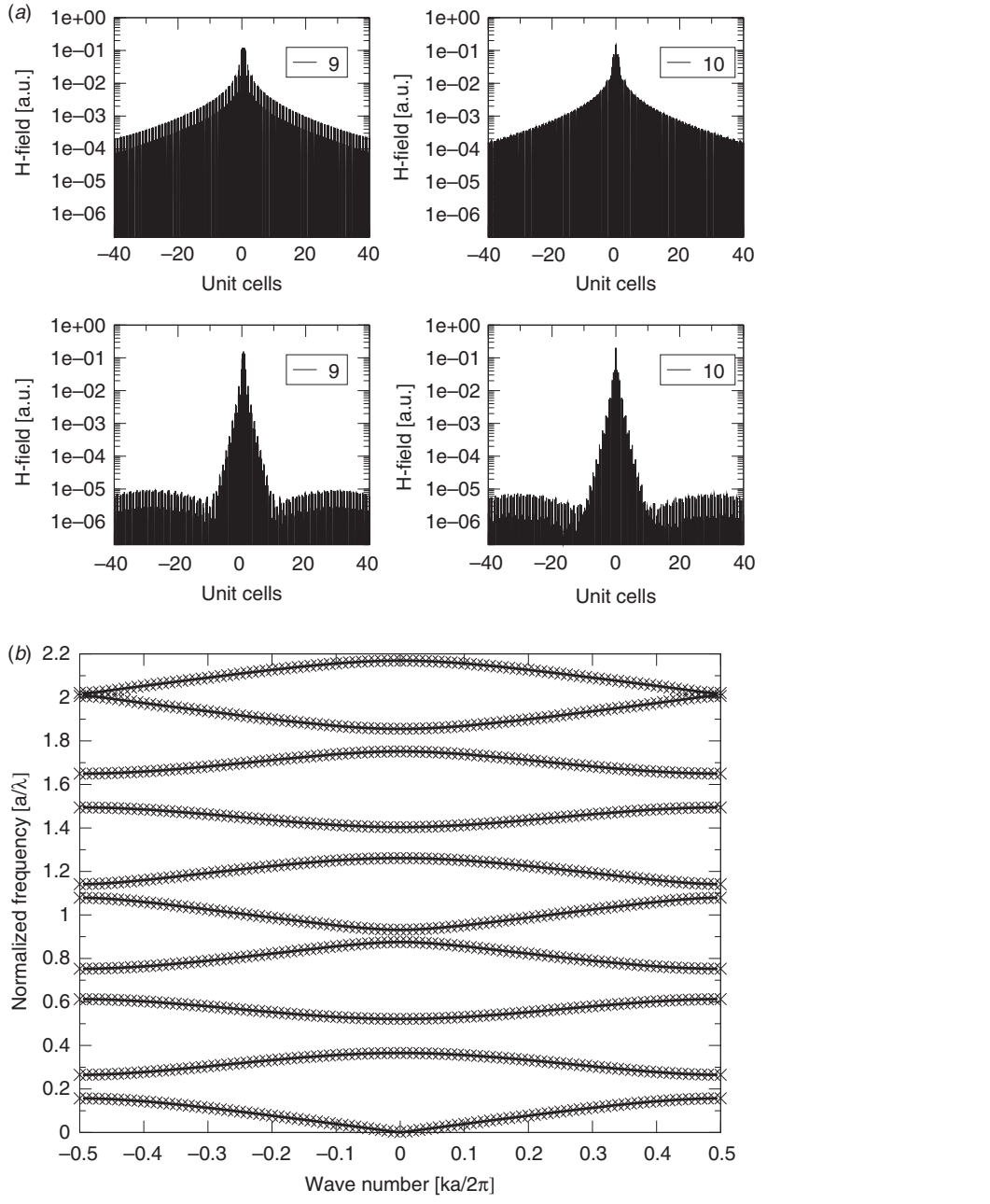

Figure 2. Magnetic Wannier functions (*a*) for bands 9 and 10 and corresponding photonic band structure for the 1D model PhC. The first row depicts the WFs that result from minimizing the spread functional for the individual bands and the second row corresponds to the case where the bands are allowed to hybridize, i.e. when the spread functional is minimized for the group consisting of bands 9 and 10. In the latter case the band index label loses its association with the physical band structure depicted in panel (*b*). This photonic band structure has been computed with the MPB package (solid lines; see [25]) and has also been reconstructed from the set of magnetic-field WFs (crosses) via Equation (6).

for bands 9 and 10 as well as the corresponding photonic band structure for our model system. From Figure 2(*b*), we derive that the energetic separation between bands 9 and 10 is extremely small. As a result, if we construct the WFs for bands 9 and 10 by separately minimizing the spread, Equation (5), we obtain poorly localized WFs as shown in the upper row of Figure 2(*a*). There, the levelling-off of the WFs for large values of $|x|$ is the result of the finite number of k-points used in the WF-construction according to Equation (2). However, if we, instead, treat bands 9 and 10 as a band complex and allow for their

hybridization, we obtain significantly improved localization properties as depicted in the second row of Figure 2(*a*). In this case, the levelling-off of the WFs for large values of $|x|$ is most probably the result of the finite accuracy with which the Bloch functions have been computed.

At this point, we would like to emphasize two important issues. First, while the information content of the WFs in the first and second row of Figure 2(*a*) is identical, the usefulness of these two sets of WFs in numerical computations is quite different as discussed below. Second, the above behavior represents a generic behavior of WFs that persists to 2D and 3D systems. The localization and symmetry properties of WFs sensitively depend on an appropriate grouping of bands and the accuracy of the Bloch functions from which they are constructed.

After having constructed the WFs for our 1D model PhC, we can now move to the description of deviations from the perfect periodicity of the ideal PhC. To this end, we decompose the dielectric constant of the PhC with defects $\epsilon(x) = \epsilon_{\mathrm{per}}(x) + \delta\epsilon(x)$ into the dielectric constant of the perfectly periodic PhC $\epsilon_{\mathrm{per}}(x)$ and the part $\delta\epsilon(x)$ that describes the deviations from perfect periodicity. Upon expanding the electric and magnetic field as well as the source terms into the corresponding WF basis, inserting these expansions into the wave equations (1), and projecting the resulting equations onto the set of WFs (Galerkin approach), we arrive at the central equation of the WF approach

$$\sum_{n'R'} \left(C^{(E/H)}_{nn',RR'} + D^{(E/H)}_{nn',RR'} - \lambda^{(E/H)} A^{(E/H)}_{nn',RR'} \right) c^{(E/H)}_{n'R'} = s^{(E/H)}_{nR}. \tag{6}$$

In this equation, the sets of coefficients $c^{(E/H)}_{nR}$ and $s^{(E/H)}_{nR}$ denote the vector of expansion coefficients of the electric or magnetic field, $E(x)$ or $H(x)$ and the vector of expansion coefficients of the source term $S^{(E/H)}(x)$, respectively. The matrices entering Equation (6) are

$$\lambda^{(E)} = \frac{c^2}{\omega^2} \quad \text{or} \quad \lambda^{(H)} = \frac{\omega^2}{c^2}, \tag{7}$$

$$A^{(E)}_{nn',RR'} = \left\langle W^{(E)}_{nR} \middle| \partial_x^2 \middle| W^{(E)}_{n'R'} \right\rangle \quad \text{or} \quad A^{(H)}_{nn',RR'} = \left\langle W^{(H)}_{nR} \middle| W^{(H)}_{n'R'} \right\rangle, \tag{8}$$

$$C^{(E)}_{nn',RR'} = \left\langle W^{(E)}_{nR} \middle| \epsilon_{\mathrm{per}}(x) \middle| W^{(E)}_{n'R'} \right\rangle \quad \text{or}$$
$$C^{(H)}_{nn',RR'} = \left\langle W^{(H)}_{nR} \middle| \partial_x \frac{1}{\epsilon_{\mathrm{per}}(x)} \partial_x \middle| W^{(H)}_{n'R'} \right\rangle, \tag{9}$$

$$D^{(E)}_{nn',RR'} = \left\langle W^{(E)}_{nR} \middle| \delta\epsilon(x) \middle| W^{(E)}_{n'R'} \right\rangle \quad \text{or}$$
$$D^{(H)}_{nn',RR'} = \left\langle W^{(H)}_{n\vec{R}} \middle| \partial_x \frac{-\delta\epsilon(x)}{\epsilon(x)\epsilon_{\mathrm{per}}(x)} \partial_x \middle| W^{(H)}_{n'\vec{R}'} \right\rangle. \tag{10}$$

The matrix $D^{(E/H)}_{nn',RR'}$ is – for both wave equations – a sum of terms over those unit cells of the PhC structure that contain a deviation from perfect periodicity. These unit cells are uniquely identified through the corresponding set of lattice 'vectors' R_{def}, so that this matrix can be expressed in terms of individual defects as

$$D^{(E/H)}_{nn',RR'} = \sum_{R_{\mathrm{def}}} B^{(E/H)}_{nn',(R-R_{\mathrm{def}})(R'-R_{\mathrm{def}})}. \tag{11}$$

Here, the matrix elements $B^{(E/H)}_{nn',(R-R_{\mathrm{def}})(R'-R_{\mathrm{def}})}$ can be precomputed for certain prototypical defects as described in [11].

The central equation of the WF approach, Equation (6), may be utilized for a number of different computations of PhC structures. For instance, we may specify a source and solve the resulting system of linear equations for the Wannier coefficients $c^{(E/H)}_{n'R'}$ of the electric or magnetic field distributions. These field distributions completely characterize the state of the electromagnetic field and may then be processed to yield further physical quantities such as the energy density, the energy flux (Poynting vector), and transmission and reflection coefficients. These types of computations will be discussed in Section 3. In the absence of sources, Equation (6) represents an eigenvalue problem for the eigenfrequency ω and the associated eigenvectors yield the eigenmodes in the WF representation.

The localized nature of the WFs leads to matrix elements that quickly decay with increasing distance $|R - R'|$ between the unit cells R and R' associated with the different WFs. As a result, we may set to zero all matrix elements for which the separation $|R - R'|$ exceeds a certain maximum range $R_{\max}$. Together with the usage of a maximum number $N_{\max}$ of bands, this implies that the matrices in Equation (6) become sparse such that advanced numerical methods for sparse systems can be employed. For our computations, we typically solve the system of linear equations, Equation (6), using a sparse-matrix LU-decomposition as available in the PARDISO package [26]. In addition, the matrix elements themselves (see Equations (8)–(11)) have to be determined numerically and this is the reason why we have refrained from writing $\delta_{nn'}\delta_{RR'}$ instead of $C^{(E)}_{nn',RR'}$ and $A^{(H)}_{nn',RR'}$. Specifically, we can compute (and store) the WFs only on a finite spatial domain. This domain is determined by the inverse of the k-point spacing used in the numerical integration of Equation (2) as the finite number of k-values inevitably induces recurrence effects as a function of the spatial coordinate x. Thus, a comparison of $C^{(E)}_{nn',RR'}$ and $A^{(H)}_{nn',RR'}$ with $\delta_{nn'}\delta_{RR'}$ provides a first idea of the quality of the WFs. Consequently, the total accuracy (and efficiency) of

WF computations depends on the accuracy of the integration schemes of Equations (8)–(10), the maximum number of bands $N_{\max}$, the value of $R_{\max}$, and the accuracy with which the WFs are determined (k-space integration scheme and spatial resolution of the numerically determined Bloch functions in Equation (2)).

We find that the reconstruction of the photonic band structure of the ideal PhC via Equation (6) provides an excellent first test for the accuracy of WF computations – specifically in the case of 2D and 3D WF computations. In Figure 2(b), we display a comparison of the reconstructed band structure for our model system with the results obtained from ordinary photonic band stucture computations. Here, we obviously use $\delta\epsilon(x) \equiv 0$ and we employ the framework described in [27] for determining the band structure via WFs. A more stringent second test that also involves $\delta\epsilon(x)$ is the computation of simple cavity structures in ideal PhCs. In Figure 3, we display the convergence characteristics of WF computations for a simple cavity structure that is obtained by replacing a single silicon layer in our 1D model PhC with an air layer. This defect creates localized cavity modes with frequencies in the photonic band gaps and we have computed the frequency of the cavity mode in the third band gap – the analytically obtained reference value is $a/\lambda = 0.6830$.

We observe that the electric-field based WF computations exhibit a much better performance than the magnetic-field based WF computations. This is a direct consequence of the before-mentioned behaviour of the electric and magnetic field at material interfaces. In fact, replacing the silicon layer with an air layer changes the original boundary conditions at the two silicon–air interfaces to continuously differentiable fields at the new (actually non-existent) air–air interfaces – both for the electric and the magnetic field. However, while the electric-field WFs exhibit continuous first derivatives across these interfaces, the magnetic-field WFs do not (see discussion above). As a consequence, representing continuously differentiable fields is comparatively more difficult in the magnetic-field formulation and this leads to a slower convergence rate relative to the electric-field formulation.

In the next section, we proceed to a discussion of the WF approach for 2D PhC structures where the basic features discussed above will reappear.

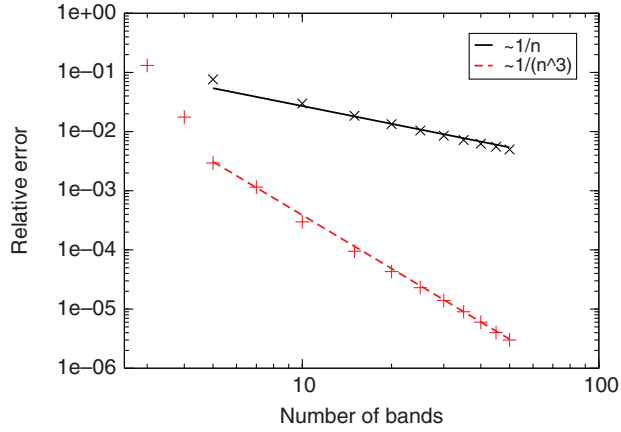

Figure 3. Convergence characteristics of WF computations for a simple cavity structure for different maximum numbers of bands. The structure consists of the replacement of a single silicon layer with an air layer in the otherwise ideal 1D model PhC. The computations have been carried out within the magnetic field formulation (crosses; the solid line represents a guide to the eye) and the electric field formulation (pluses; the dashed line represents a guide to the eye) of the WF approach ($R_{\max} = 10$) for the cavity mode within the third band gap with frequency $a/\lambda = 0.683$. (The color version of this figure is included in the online version of the journal.)

3. Wannier function computations of 2D photonic crystal structures

Two-dimensional PhC structures are defined by a strict homogeneity of the system in z-direction, i.e. light propagates in the xy-plane and the dielectric constant $\epsilon(\vec{r})$, $\vec{r} \equiv (x, y)$, too, varies only in the xy-plane. In this case, the two (linear) polarizations of the electromagnetic field decouple and instead of a vectorial wave equation, we can consider two separate scalar problems. Nevertheless, the basic notations introduced in Section 1 can be directly transferred and/or straightforwardly generalized to 2D (and 3D) problems. For the case when the polarization of the electric field is parallel to the z-axis, i.e. when $\vec{E}(\vec{r}) = (0, 0, E(\vec{r}))$ and the magnetic field components lie in the xy-plane, we obtain the wave equation for E-polarized radiation as

$$\left[\partial_x^2 + \partial_y^2\right] E(\vec{r}) + \frac{\omega^2}{c^2}\,\epsilon(\vec{r})\,E(\vec{r}) = S^{(E)}(\vec{r}). \tag{12}$$

Similarly, in the case when the polarization of the magnetic field is parallel to the z-axis, i.e. when $\vec{H}(\vec{r}) = (0, 0, H(\vec{r}))$ and the electric field components lie in the xy-plane, we obtain the wave equation for H-polarized radiation as

$$\left[\partial_x\left(\frac{1}{\epsilon(\vec{r})}\,\partial_x H(\vec{r})\right) + \partial_y\left(\frac{1}{\epsilon(\vec{r})}\,\partial_y H(\vec{r})\right)\right] + \frac{\omega^2}{c^2} H(\vec{r}) = S^{(H)}(\vec{r}). \tag{13}$$

In these expressions, $S^{(E)}(\vec{r})$ and $S^{(H)}(\vec{r})$ denote corresponding source terms. In addition, we would like to note that the Equations (12) and (13) have been derived from the Maxwell curl equations alone.

Owing to our assumption of the homogeneity along the z-axis, the solutions to these equations automatically also satisfy the Maxwell divergence equations.

The apparent mathematical similarity of Equations (12) and (13) with their 1D counterparts (see Equation (1)), leads to similar behavior of the respective solutions. For instance, while for E-polarized fields the continuity conditions across a material interface are that both the field and its first derivative are continuous, for H-polarized fields the continuity conditions are that the field is continuous with a discontinuity in the first derivative, which depends on the dielectric contrast (see Section 1). Therefore, at this point we can already anticipate that the WF approach for E-polarized radiation exhibits rather different convergence characteristics when compared with the WF approach for H-polarized radiation.

Putting this aside, in 2D there exist substantial physical differences between the different polarizations. In particular, for E-polarized fields, the existence of a 2D photonic band gap is favored in systems where scatterers with a high value of the dielectric constant are embedded in a matrix with a low value of the dielectric constant, notably in the square lattice (lattice constant a). For H-polarized radiation, the situation is reversed and hexagonal lattices with low-dielectric inclusions in a connected high-dielectric network exhibit the largest photonic band gaps. In Figure 4, we display the photonic band structures of two model 2D PhC systems that will provide the basis for our subsequent discussions. In particular, the square array of silicon posts exhibits a large photonic band gap for E-polarized radiation that extends from $a/\lambda = 0.297$ to $a/\lambda = 0.442$. Similarly, the hexagonal array of air pores in silicon exhibits a large photonic band gap for H-polarized radiation that covers the range form $a/\lambda = 0.301$ to $a/\lambda = 0.492$.

The construction of WFs for higher-dimensional PhCs is considerably more involved than that for 1D PhCs for two interrelated reasons. First, higher-dimensional PhCs fail to provide energetically isolated groups of bands especially for higher frequencies. For our model PhC structures this is the case for all bands above the third band gap. There, all the bands become entangled so that the original algorithm [10] has to be extended in order to account for this band entanglement. Fortunately, such an extension has been developed within electronic structure theory [28] and can be adapted to PhC-related problems. Perhaps the most important ingredient of this extension is the appropriate grouping of bands that has been mentioned in Section 1. However, this ties into the second aspect related to higher-dimensional PhCs. These PhCs exhibit much richer symmetry properties and this

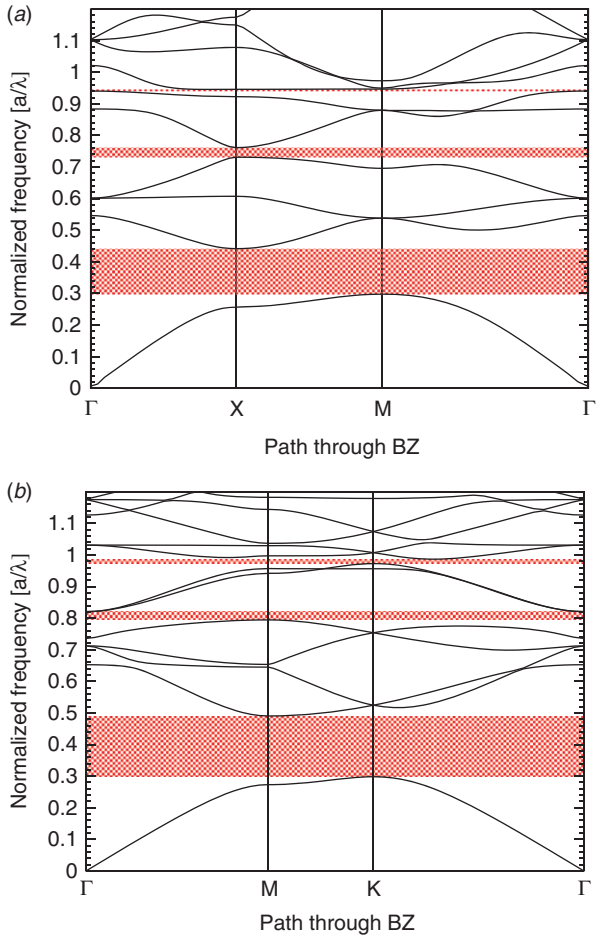

Figure 4. Photonic bandstructures for different 2D PhC systems that exhibit particularly large photonic band gaps (shaded areas). (*a*) E-polarized radiation in a square lattice of silicon posts ($r/a = 0.18$) in air; (*b*) H-polarized radiation in a hexagonal lattice of air pores ($r/a = 0.45$) in a silicon matrix. (The color version of this figure is included in the online version of the journal.)

directly leads to a much richer behavior regarding the allowed WF symmetries and localization centers (see Figure 5).

Specifically, the symmetries of exponentially localized WFs are determined by the symmetries of Bloch modes at the high-symmetry points of the BZ, from which the WFs are constructed. Exponential localization may be achieved, when the generalized Bloch functions (through the unitary transformations $U_{nn'}(\vec{k})$ – see Equation (2)) can be chosen such that they are analytic for complex valued wave vectors $\vec{k}$ [22,29,30]. Clearly, for this to work, it is a necessary prerequisite to have continuously varying Bloch functions for real wave vectors $\vec{k}$ everywhere inside the BZ and across the edges into neighboring (i.e. higher) BZs. In turn, this can be accomplished by a proper choice of symmetric WFs for closed groups of bands [31,32].

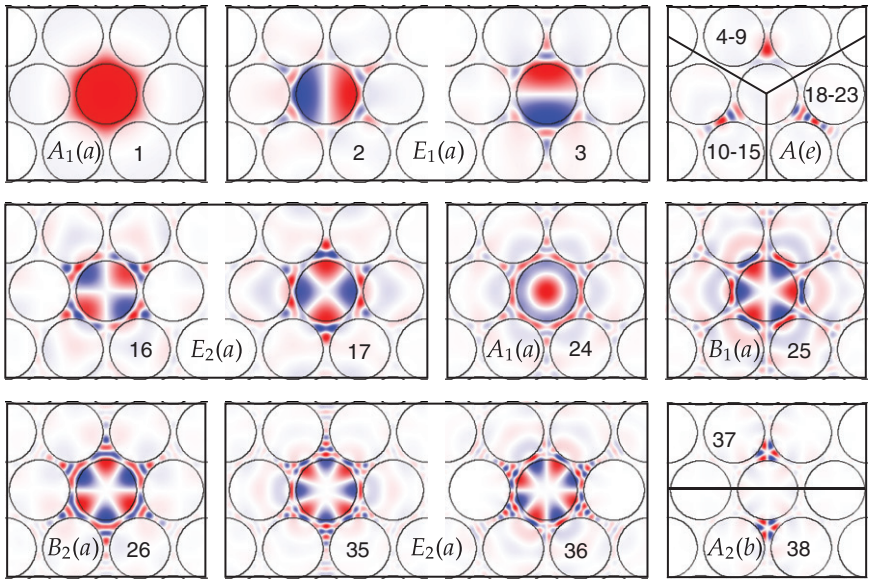

Figure 5. Photonic WFs for H-polarized radiation in the 2D model PhC whose band structure is displayed in Figure 4(*b*). The legend denotes the generalized band index. The WFs associated with bands 4–9, 10–15, and 18–23, respectively, can be obtained from the three representative functions displayed in the upper right box of the figure through five successive 60° rotations. For instance, the set of WFs 4–9 forms a sixfold star, where each spike of the star is identical to the (suitably rotated) WF shown. All these WFs exhibit certain symmetries and the corresponding irreducible representations are indicated (see text for further details). (The color version of this figure is included in the online version of the journal.)

Then, the WFs form representations of the site symmetry groups associated with their respective center of localization. This site symmetry group consists of all symmetry operations of the space group that leave the center of localization invariant in space, modulo a translation by a lattice vector. Hence, the Wannier functions can be classified with respect to the particular representations they form for their respective site symmetry group. Based on this, the possible localization centers within one Wigner–Seitz cell can be labeled by the Wyckoff letters [33], where each site symmetry group is isomorphous to a point subgroup of the point group of the underlying PhC. This subgroup's irreducible representations are used to classify the WFs. For the hexagonal lattice, the respective pointgroups are $C_{6v}(a,\Gamma), C_{4v}(c,M)$, and $C_{3v}(b,K)$, where we have used the notation described in Ref. [34].

In Figure 5, we depict some of the WFs for H-polarized radiation in the 2D hexagonal model PhC whose band structure is shown in Figure 4. All these WFs correspond to the Wigner–Seitz cell centered at the origin, i.e. they carry the lattice-vector label $\vec{0}$. They have been constructed along the lines of the (preprocessing) arguments outlined above and with the help of the algorithm of [28]. Their symmetry and localization properties are clearly visible. In order to achieve these excellent localization properties, different localization centers (or in the language of [10,28] different Wannier centers) have been employed. These WFs have been obtained from Bloch functions with a spatial resolution of 96×96 points within the primitive unit cell (via the MPB package [25]) that have been computed for an 11×11 Monkhorst-Pack mesh [35] of *k*-points within the BZ.

With these WFs in hand, we now proceed to a discussion of the accuracy of the WF approach regarding the description of cavity modes associated with simple defect structures in 2D PhCs. As a matter of fact, for E-polarized radiation excellent convergence characteristics have already been obtained and typically only a few (up to 10) WFs are required [11]. However, and as discussed above, for H-polarized radiation the situation is quite different due to different boundary conditions for the tangential magnetic field across material interfaces. In Figure 6, we display our results for the eigenfrequencies of cavity modes lying in the first band gap of our hexagonal model 2D PhC when a single pore is filled with a material with dielectric constant ϵ_{def} (for a discussion of how to extend Equation (6) to the 2D case, we refer to the discussion around Equations (14) and (15) below).

For low values of ϵ_{def}, doubly degenerate dipole modes separate from the upper band ('donor modes') and move deeper into the photonic band gap as ϵ_{def} is increased. For still higher values of ϵ_{def}, doubly degenerate quadrupole modes, a second-order monopole mode, and finally a hexapole mode emerge.

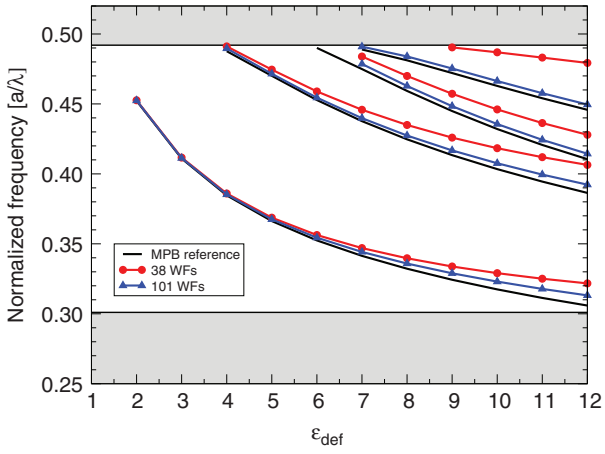

Figure 6. Cavity mode frequencies in the first band gap for H-polarized radiation in the hexagonal 2D model PhC (see Figure 4(*b*) for the corresponding band structure). The cavity is created by filling a single pore of the ideal PhC with a material with dielectric constant ϵ_{def}. The reference solution (solid line) has been obtained with the help of supercell computations using the MPB package (see the text for a discussion of the accuracy near the band edges). The WF computations have been carried out with 38 WFs (triangles) and 101 WFs (circles), respectively. (The color version of this figure is included in the online version of the journal.)

They, too, move deeper into the photonic band gap as ϵ_{def} is increased. In Figure 6, we show as a reference solution (solid line) the results of supercell computations using the MPB package [25]. Owing to the limited size of the supercell that can be handled, we do not expect to obtain good reference values for cavity frequencies in close proximity to the photonic band edge. The corresponding WF computations have been carried out using $R_{\max} = 5a$ with 38 WFs (triangles) and 101 WFs (circles), respectively. For cavity frequencies away from the band edge, we observe very good agreement between the different computations. More precisely, for the dipole and quadrupole modes, we find excellent agreement for low and moderate values of ϵ_{def} already for the 38-band WF computations. However, for large values of ϵ_{def}, notably for the second-order monopole and the hexapole modes, the accuracy of the 38-band WF computation is less satisfactory. This deficiency is largely removed by increasing the number of WFs used in the computations; when using 101 WFs, we find very good agreement for all values of ϵ_{def} (averaged over the different modes, less than 3% error relative to the MPB results for $\epsilon_{\text{def}} = 12$). This improved convergence can be traced back to the fact that the set of WFs for bands 39–101 features additional WFs with higher-order multipole-like profiles that are compatible with the symmetries of the cavity modes and lead to an improved representation of the associated cavity mode profiles, in particular in the thin veins between the air pores and at the material interfaces.

Therefore, we arrive at the following intermediate conclusion regarding the state of WF computations in 2D PhCs. The treatment of E-polarized radiation is very efficient and a few WFs suffice to achieve excellent accuracy. As a result, such computations have been used to develop novel device concepts [14–16] to advance computation and analysis methodologies such as small-rank update procedures [16] and WF-based sensitivity analysis tools [17], and to explore alternative construction methods for localized Wannier-like basis functions [36] that are easier to compute and would still fit into the overall WF framework for computing PhC structures. On the other hand, the treatment of H-polarized radiation is considerably more challenging. Nevertheless, and despite different suggestions earlier [18], accurate results can be achieved with the help of maximally localized WFs. Admittedly, the construction of these maximally localized WFs requires considerable effort as described above. In view of the increased number of bands that have to be used for H-polarized radiation, these maximally localized WFs represent a *sine qua non* for realizing an efficient computational scheme because only they guarantee the required symmetries and sparsity properties of the corresponding matrices. Consequently, further work has to be aimed at reducing the number of WFs that is required for obtaining accurate results with predictive power for experiments. For instance, this could be accomplished by determining which of the higher-band WFs contribute the most to the above-mentioned simple cavity modes. This can be accomplished through the *V*-parameter introduced in [11]. Then, retaining only the relevant WFs could considerably reduce the numerical effort, while still providing accuracies comparable to the 101-band WF computations depicted in Figure 6. Finally, we want to note that our model system for H-polarized radiation, with its thin veins and large dielectric contrast, represents a fairly demanding problem not only for the WF approach but also for most other numerical methods and, therefore, provides a benchmark problem for PhC computations.

The WF approach is particularly useful for the efficient description of waveguiding structures embedded in PhCs. These systems provide a novel platform for realizing integrated optics [3]. Consequently, a significant amount of conceptual and methodical work [9,11,16,17,19] has been completed, which turns the WF approach into an efficient forward solver for optimization methodologies [16,17] and large-scale circuit theory approaches [27]. We illustrate this by considering the realization of integrated photonic

circuits via infiltrating individual pores of our 2D model PhC of a hexagonal lattice of air pores in silicon with low-dielectric-constant materials. The resulting circuits offer a number of advantages over more traditional systems that involve missing pores or pores with different diameters and/or at different locations. First, such hybrid and multi-component systems exhibit considerably more flexibility regarding the design of functional elements. A single low-dielectic infiltrated pore supports fewer cavity modes than a missing pore. As a result, it is considerably easier to realize a broad-band single mode waveguide by infilling a row of pores (see Figure 7), which is the primary basis for the rational design of more complex functionalities. Secondly, many low-dielectric-constant materials are organic materials, such as polymers and liquid crystals, and are – in contrast to silicon – highly susceptible to applied (external) electric and magnetic fields. Therefore, the resulting photonic circuits may be engineered to exhibit a considerable degree of electro- and/or magneto-optical tunability. In addition, most materials in this class also exhibit a strong nonlinear optical response and this makes composite systems very attractive for applications as active elements. As a result, such hybrid PhC structures that combine an inorganic PhC backbone with the infiltration of tunable and/or optically active materials may substantially enhance their technological utility, over and above that of either material by itself [14,37,38]. In addition, based on today's micro-fabrication capabilities regarding such hybrid systems, the concept of rewritable PhCs and rewritable PhC-based optical circuitry has been developed [39] and the last four years has seen a tremendous increase in experimental activities [39–47].

In order to account for optical anisotropy, we have to extend our WF-formalism to tensorial dielectric constants. In the simplest case of in-plane anisotropy, i.e. when $\epsilon_{xz} = \epsilon_{yz} = \epsilon_{zx} = \epsilon_{zy} = 0$, the separation of polarization discussed before remains intact and we only have to modify the equation for the H-polarization to

$$\begin{pmatrix} \partial_y \\ -\partial_x \end{pmatrix} \cdot \left[\begin{pmatrix} \epsilon_{xx}(\vec{r}) & \epsilon_{xy}(\vec{r}) \\ \epsilon_{yx}(\vec{r}) & \epsilon_{yy}(\vec{r}) \end{pmatrix}^{-1} \cdot \begin{pmatrix} \partial_y \\ -\partial_x \end{pmatrix} H(\vec{r}) \right] + \frac{\omega^2}{c^2} H(\vec{r}) = S^{(H)}(\vec{r}). \quad (14)$$

Even in this case, the central equation of the WF approach, Equation (6) together with Equations (8)–(11), may be utilized except for the minor replacement of the scalar lattice 'vectors' R and R' by 2D lattice vectors $\vec{R}$ and $\vec{R}'$. If we further assume that the ideal PhC is made from isotropic materials only, the

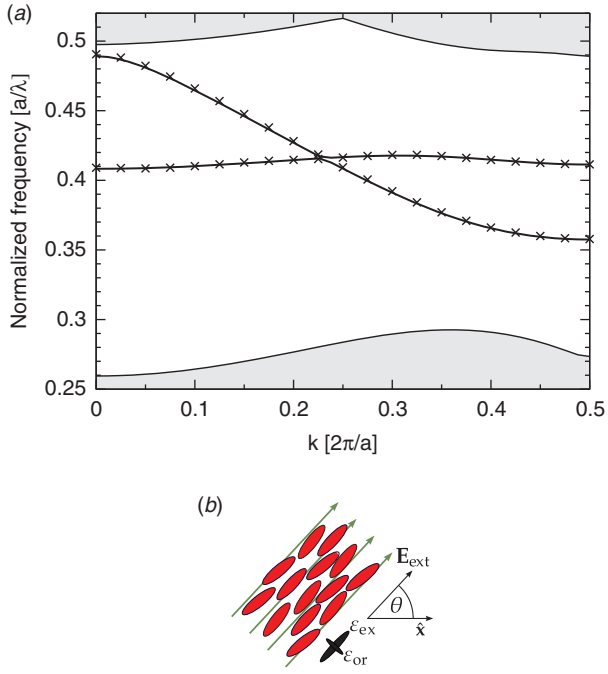

Figure 7. Dispersion relation (*a*) of a broad-band single-mode waveguide that is inscribed into a 2D PhC of air pores in silicon. The waveguide is realized by infilling a row of pores with a low-dielectric-constant material ($\epsilon = 2.89$) such as a polymer. The results of the WF-based computations (crosses) are in excellent agreement with MPB-based reference computations. If the pores are filled with a liquid crystal (*b*), an external (quasi-static) electric field E_{ext} (arrows) may reorient the molecules (cigar-shaped objects) as described by the angle θ of the nematic director (cigar-shaped symbol with cross-piece). This provides a tunable waveguide dispersion that is based on the differences between the ordinary and extraordinary dielectric constant (ϵ_{or} and ϵ_{ex}) along and perpendicular to the orientation of the nematic director field, respectively (see Figure 8(*a*)–(*d*)). (The color version of this figure is included in the online version of the journal.)

D-matrix elements have to be significantly modified to accommodate the optical anisotropy of the infiltrated materials according to

$$D^{(H)}_{nn',\vec{R}\vec{R}'} = \langle W^{(H)}_{n\vec{R}} | \begin{pmatrix} \partial_y \\ -\partial_x \end{pmatrix} \cdot \left[\begin{pmatrix} \epsilon_{xx}(\vec{r}) & \epsilon_{xy}(\vec{r}) \\ \epsilon_{yx}(\vec{r}) & \epsilon_{yy}(\vec{r}) \end{pmatrix}^{-1} - \begin{pmatrix} \epsilon_{\text{per}}(\vec{r}) & 0 \\ 0 & \epsilon_{\text{per}}(\vec{r}) \end{pmatrix}^{-1} \right] \cdot \begin{pmatrix} \partial_y \\ -\partial_x \end{pmatrix} | W^{(H)}_{n'\vec{R}'} \rangle. \quad (15)$$

The remaining matrix elements of the A- and C-matrices require only the minimal changes of extending the integration domain to 2D (A- and C-matrices) and replacing the 1D operator that only features x-derivatives by the corresponding 2D

operator that features a sum of this 1D operator and an analogous 1D operator where the x-derivatives are replaced by y-derivatives (C-matrix only; cf. also Equation (13) with the l.h.s. expression in Equation (1)).

In Figure 7(a), we display the dispersion relation of such a broad-band single-mode waveguide that is obtained when filling a row of pores of our 2D model PhC with an isotropic material with dielectric constant $\epsilon = 2.89$ (polymer). A similar waveguide dispersion relation, albeit with a shifted lower cut-off frequency, may be obtained when infilling with an isotropic material with dielectric constant $\epsilon = 2.25$. Both waveguides exhibit a similar mode structure. In particular, the two waveguide branches correspond to modes with even (wide frequency range) and odd (narrow frequency range) mode profiles with respect to the waveguide's symmetry axis. As a result, the electric field distributions associated with these modes probe different directions in space.

Hence, if the pores were filled with a liquid-crystalline material, the response of these modes to the orientation of the nematic director is quite different [38]. For instance, if the nematic director is aligned with the waveguide axis, the even and odd modes effectively experience the dielectic constant associated with the ordinary axis and extraordinary axes, ϵ_{or} and ϵ_{ex}, respectively. The opposite statement applies if the nematic director is aligned perpendicular to the waveguide axes. For oblique orientations, an interaction between these waveguide modes develops and its strength depends on the difference between ordinary and extraordinary dielectric constants and the relative orientation of the nematic director relative to the waveguide axis. As a result, mode mixing occurs and the waveguide dispersion relation may be tuned. In Figure 8, we display the results of this dispersion relation tuning for realistic values $\epsilon_{or} = 2.25$ and $\epsilon_{ex} = 2.89$ of the liquid crystalline material properties, e.g. the liquid crystal E7. In particular, upon reorienting the nematic director from $\theta = 0^\circ$ to $\theta = 90^\circ$, we observe (i) a tunable cut-off frequency of the predominantly even mode [38] and a corresponding tunability of the slow-light regime as well as (ii) the opening and closing of a mini gap as a result of an avoided crossing between the hitherto non-interacting waveguide modes. In addition, we observe the aforementioned differences between the two highly-symmetric orientations of the nematic director – in both cases the interaction between the even and odd modes is switched off but they effectively interchange the roles regarding the ordinary and extra-ordinary dielectric constants.

This concept of tunable waveguide dispersion relations has been further developed into designs for simple tunable beam-splitters [38,46]. In Figure 9, we depict the schematic set-up of a more sophisticated tunable beam-splitter design based on several isotropic low-dielectric-constant materials and a segment of a liquid-crystal based tunable waveguide. This design has been carefully engineered and optimized with the help of a WF-based circuit theory for large-scale PhC structures [27] that utilizes a guided-mode scattering matrix formalism [48]. In Figure 10, we display the corresponding device characteristics regarding the tuning of the transmittance between bar and cross port. By changing the orientation of the nematic director from $\theta = 48^\circ$ to $\theta = 90^\circ$, the transmittance can be switched from near-100% transmittance into the bar port to a near-100% transmittance into the cross port over a broad frequency range that lies within the range of single-mode operation of the connecting waveguides. In addition, we observe low values of the reflectance (less than 1%) back into the input port over this frequency range and for all angles θ of the nematic director's orientation.

A detailed discussion of the operation principle of this device is outside the scope of the present review article. However, we would like to note that for a given orientation θ of the nematic director the computation of a single transmittance spectrum (310 data points) as displayed in Figure 10 takes about 300 minutes of CPU time and requires about 8 GByte of RAM on an AMD Opteron processor with a clock speed of 2.6 GHz using 4 threads. For this computations, we have used the first 15 WFs which – for the above values of the dielectric constants – ensures an accuracy better than 1% (see Figure 6).

4. Recent developments and future directions

To date, the search for the 'Holy Grail' of flexible and inexpensive fabrication of large-scale, high-quality 3D PhCs with complete photonic band gaps at visible or near infrared frequencies, into which functional elements can be easily inscribed, has not yet produced definite results. Nevertheless, recent progress in microfabrication indicates that this 'dark age' may come to an end in the not too distant future [49]. Then, the specific advantages of the WF approach will come into full effect. Owing to the multi-resolution properties of the WFs [21], we expect a rather favorable scaling of the WF approach with increasing spatial dimensionality. More precisely, the transition from 1D to 2D systems as described in Sections 2 and 3 has resulted in about the same number of WFs that are required to obtain converged results, both in the E-field and the H-field formulations (cf. Figures 3 and 6), so that we may expect a similar behavior in 3D. A full 3D formulation requires vectorial WFs and the various

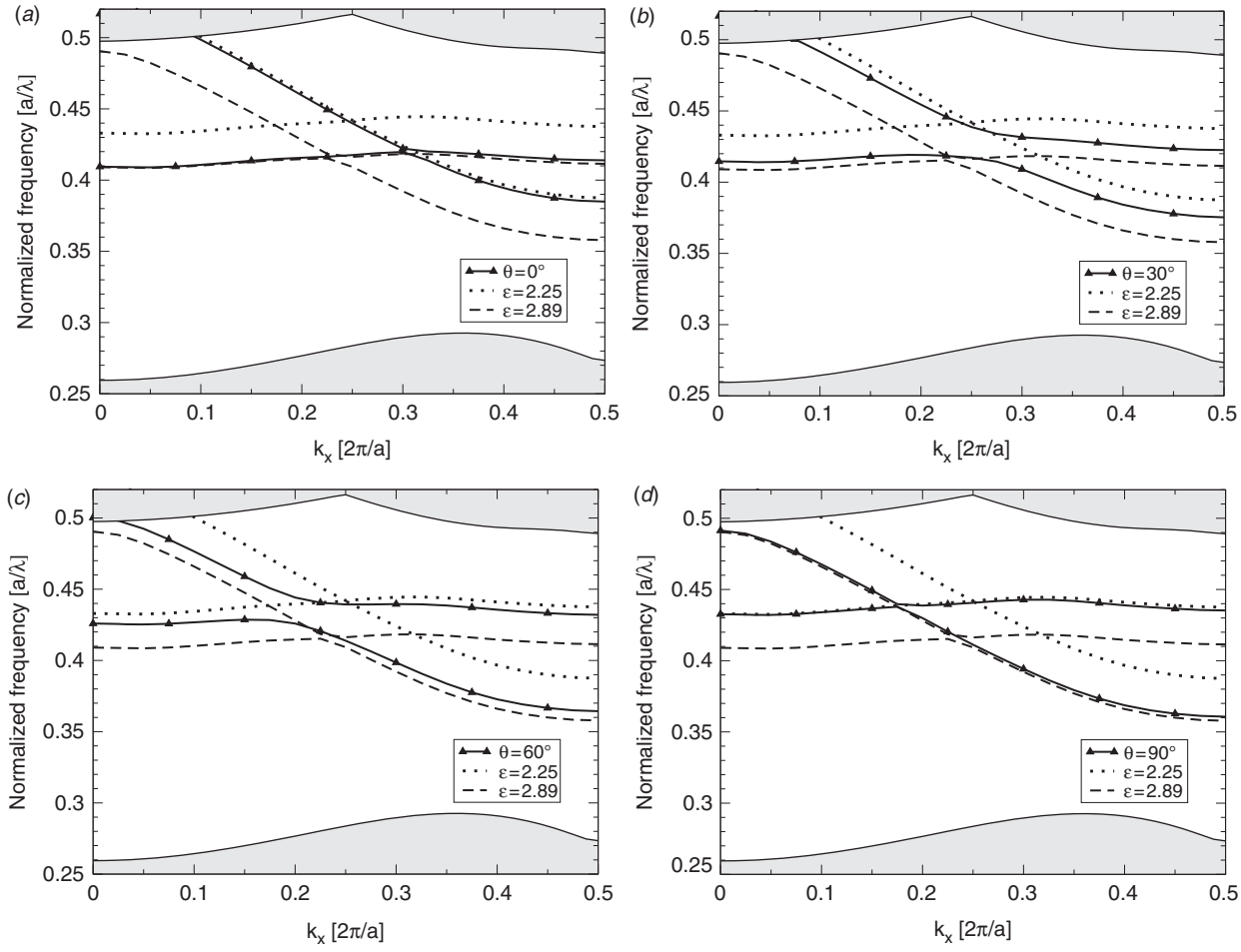

Figure 8. Tunable waveguide dispersion for a broad-band single-mode waveguide that is realized by filling the pores of a hexagonal silicon 2D PhC structure with liquid crystalline material (ordinary dielectric constant $\epsilon_{or} = 2.25$, extraordinary dielectric constant $\epsilon_{ex} = 2.89$). Depending on an external (quasi-) static field (see Figure 7(*b*)), the orientation θ of the nematic director changes and the dispersion relation may be tuned between the limits provided by the dispersion relations for waveguides made from isotropic materials with ordinary or extraordinary dielectric constants (dashed and dotted lines; see text for details).

vector components exhibit different boundary conditions at material interfaces. As a result, we anticipate that the performance characteristics of a 3D WF approach will be a mediation of the 2D E-polarized and the 2D H-polarized cases. However, the 3D case features one additional subtlety in that we now can no longer satisfy Maxwell's divergence equations from the outset. In other words, within a magnetic field formulation, the relevant equations are

$$\nabla \times \left(\frac{1}{\epsilon(\vec{r})} \nabla \times \vec{H}(\vec{r}) \right) - \frac{\omega^2}{c^2} \vec{H}(\vec{r}) = \vec{S}(\vec{r}) \quad \text{and}$$
$$\nabla \cdot \vec{H}(\vec{r}) = 0. \tag{16}$$

Corresponding statements apply to formulations based on the electric or the displacement field. However, only in a magnetic or a displacement field formulation do the WF functions and the electromagnetic fields that are associated with defect states obey the same divergence condition. Furthermore, while the set of Bloch functions obtained via the magnetic field formulation, Equation (16) including the divergence conditions, comprises a complete set of basis functions for the space of physical solutions, the set of Bloch functions obtained via a corresponding electric field formulation does not possess this property [50]. As a result, a magnetic field formulation is the preferred choice for 3D WF computations.

In Figure 11, we display the 3D WFs for a silicon woodpile PhC that exhibits a complete photonic band gap between bands 2 and 3 (see also [49] for the experimental realization of a closely related structure with a photonic band gap at 1.55 μm.). These WFs have been obtained with an extension to 3D of the group-theoretical preprocessing scheme and

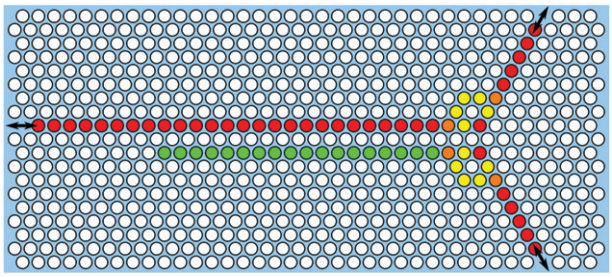

Figure 9. Schematic setup of a tunable beam-splitter based on the infiltration of individual pores with low-dielectric-constant materials of prescribed values. The input waveguide (middle left), bar waveguide (upper right), and cross waveguide (lower right) consist of pores that are filled with a low-dielectric material with isotropic dielectric constant (red; $\epsilon = 2.89$). The short waveguide segment that runs parallel to the input waveguide is realized by pores that are infilled with a liquid crystal (green; $\epsilon_{or} = 2.25, \epsilon_{ex} = 2.89$) whose nematic director field can be reoriented within the xy-plane. The pores in the coupling region are filled with low-dielectric-constant materials with $\epsilon = 2.56$ (orange) and $\epsilon = 2.40$ (yellow). (The color version of this figure is included in the online version of the journal.)

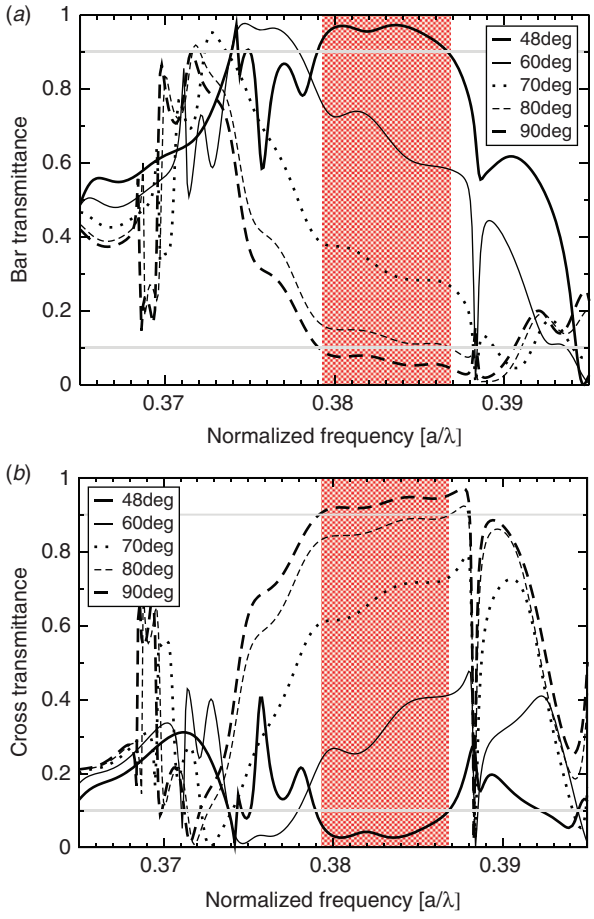

Figure 10. Performance characteristics for the tunable beam-splitter design depicted in Figure 9. Reorienting the nematic director between $\theta = 48^\circ$ and $\theta = 90^\circ$ allows us to completely switch from a near 100%-transmittance into the bar port all the way to a near 100%-transmittance into the cross port over a broad frequency range (shaded area) while at the same time maintaining low reflectance values back into the input port. (The color version of this figure is included in the online version of the journal.)

subsequent application of the algorithm of [28] as described in Section 3 for the 2D H-polarized case. The localization and symmetry properties of the WFs are clearly visible. As compared with the higher bands, the WF for the first band (and its partner for the second band) is less localized. This is the result of the linear dispersion relation in the long wavelength limit and the topological polarization singularity at $\vec{k} = \vec{0}$ associated with these bands.

These WFs have been constructed by using a $7 \times 7 \times 7$ Monkhorst-Pack mesh in the BZ and the corresponding Bloch functions have been obtained from the MPB package with a spatial resolution of $32 \times 32 \times 32$ within the unit cell. Using the 32 lowest lying 3D WFs, we have reconstructed the photonic band structure of the underlying PhC via Equation (6) and we display the results in Figure 12. We observe very good agreement between the WF-based reconstructed band structure and the reference band structure obtained via the MPB package. Based on these encouraging results, we expect that WF-based computations for 3D PhC structures will become available in the not too distant future.

Another important aspect of current PhC research is concerned with the role of disorder. Already in one of the seminal papers it has been argued that disordered PhCs provide an ideal system for the realization of Anderson localization of light [2]. In view of recent experiments on random lasing [51], it is highly attractive to extend these lines of thought on Anderson localization in disordered PhC systems with passive constituent materials to disordered PhC structures with optically active constituents. More mundane but of equal significance is the development of a detailed understanding regarding the role of fabricational disorder, notably in PhC waveguiding structures that operate in the slow light regime [52]. For such type of analyses, the natural approach is based on a Green's function formalism [53], which typically requires the Green's function (GF) of a reference system as an input. For PhCs, the natural reference system is the ideal PhC itself, so that we are faced with the task of constructing the GF within a WF-representation. Recalling our earlier statements (see Section 3) regarding the relative ease of demonstrating (and developing) novel methodologies for the case of 2D E-polarized radiation, we now slightly rewrite the corresponding

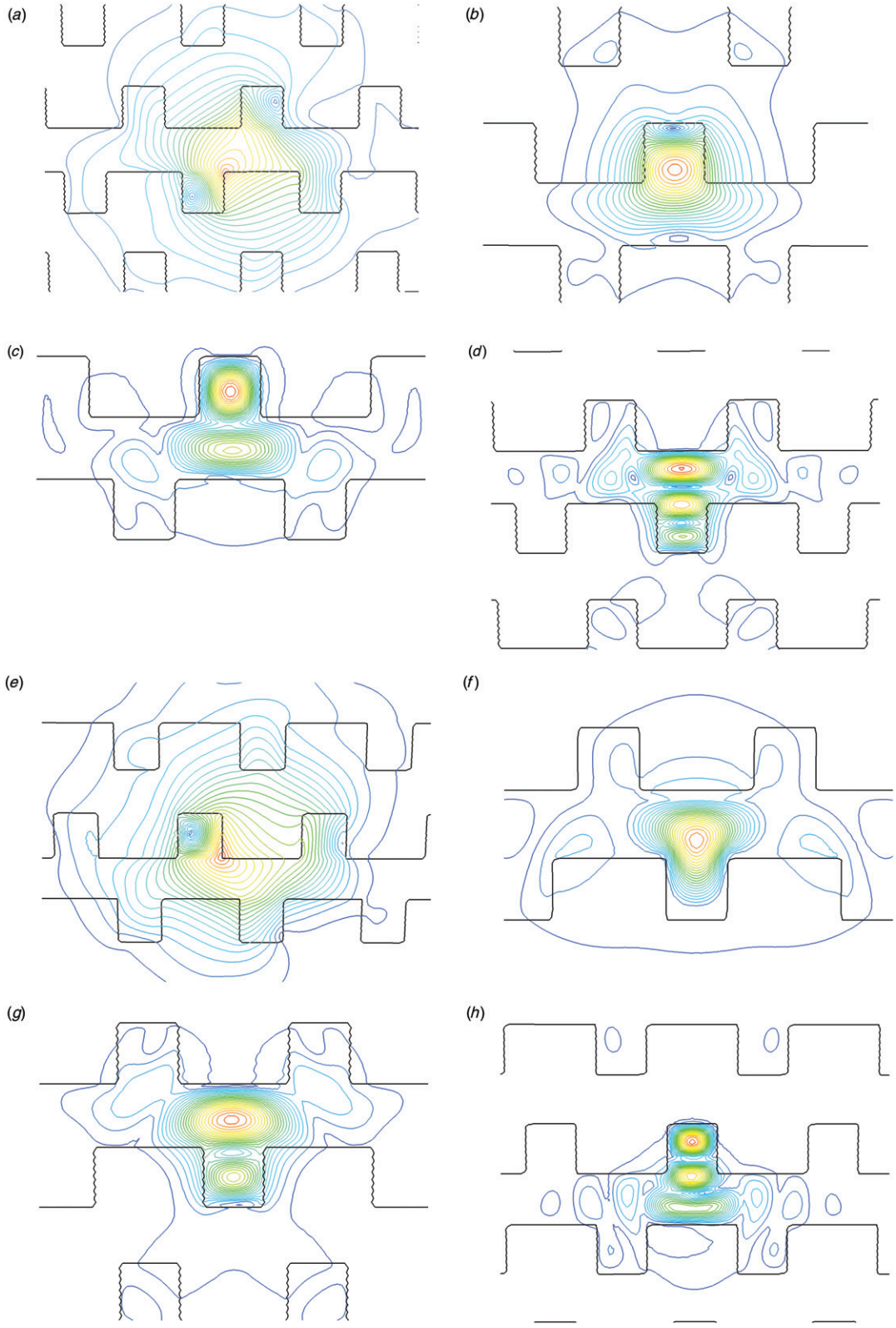

Figure 11. Maximally localized WFs for a 3D silicon woodpile structure (square rods, fcc symmetry, $\epsilon_{Si} = 12$), within the H-field formulation. The top row shows iso-contours for the absolute value of the magnetic field in a plane through the middle of one rod and the bottom row shows iso-contours of the same WFs in a plane through the middle of a rod that is perpendicular to the rod in the top row. As a guide to the eye, the silhouette of the silicon rods is displayed, too (black lines).

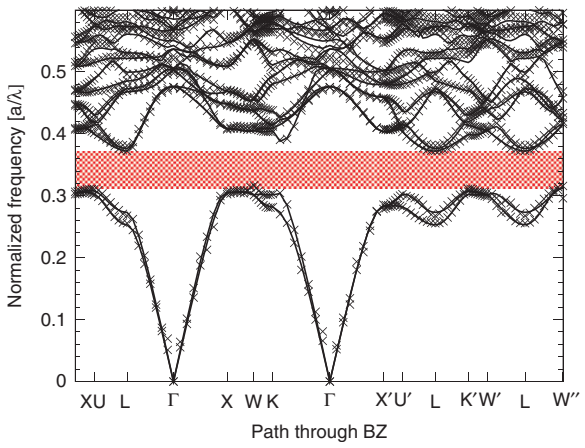

Figure 12. Photonic band structure of a silicon woodpile PhC (square rods, fcc symmetry, $\epsilon_{\mathrm{Si}} = 12$). This band structure has been obtained from the MPB package (solid lines) and has been reconstructed using the 32 lowest lying WFs (crosses), some of which are depicted in Figure 11. (The color version of this figure is included in the online version of the journal.)

wave equation (12) so that it more closely conforms to the standard notation of electronic structure theory [53]. Explicitly, we have

$$\frac{1}{\epsilon(\vec{r})}\left[\partial_x^2 + \partial_y^2\right] E(\vec{r}) + \frac{\omega^2}{c^2} E(\vec{r}) = S^{(E)}(\vec{r}), \tag{17}$$

and the GF fulfills this equation for a point-like source term of the form $S^{(E)}(\vec{r}) = \delta(\vec{r} - \vec{r}_s)$ where $\vec{r}_s$ denotes the location of the source. For an ideal PhC, i.e. when $\epsilon(\vec{r}) = \epsilon_{\mathrm{per}}(\vec{r})$, we can utilize the completeness of either the Bloch functions or the WFs and write down the GF either in Bloch function or WF representation

$$\begin{aligned} G(\vec{r}, \vec{r}_s; \omega) &= \epsilon_{\mathrm{per}}(\vec{r}_s) \sum_n \int_{\mathrm{BZ}} \mathrm{d}^2 k \, \frac{E^*_{n\vec{k}}(\vec{r}_s)\, E_{n\vec{k}}(\vec{r})}{\omega^2 - \omega^2_{n\vec{k}}} \\ &= \epsilon_{\mathrm{per}}(\vec{r}_s) \sum_{\alpha,\beta} W^*_\alpha(\vec{r}_s)\, G_{\alpha\beta}(\omega)\, W_\beta(\vec{r}). \end{aligned} \tag{18}$$

Here, $\alpha = (n\vec{R})$ and $\beta = (n'\vec{R}')$ represent composite indices that facilitate a compact notation and the 'WF structure constants' $G_{\alpha\beta}(\omega)$ are defined as

$$\begin{aligned} G_{\alpha\beta}(\omega) \equiv G_{n\vec{R};\, n'\vec{R}'}(\omega) &= \sum_m \int_{\mathrm{BZ}} \mathrm{d}^2 k \, \frac{U_{nm}(\vec{k})\, U^*_{n'm}(\vec{k})}{\omega^2 - \omega^2_{m\vec{k}}} \\ &\times \exp\left(i\vec{k} \cdot (\vec{R}' - \vec{R})\right). \end{aligned} \tag{19}$$

In view of the fact that Bloch functions can, in general, only be determined numerically, the WF representation of the GF (r.h.s. of Equation (18)) is clearly advantageous relative to the Bloch representation (middle of Equation (18)). In particular, in the WF representation, the detailed information within a unit cell is described via the WFs themselves so that the structure constants only have to be computed for the lattice sites. Furthermore, the Toeplitz-properties of the structure constants allow for the usage of efficient (sparse) storage schemes. If we were to work with the Bloch functions representation instead, we would have to store Bloch functions for many wave vectors $\vec{k}$ within the BZ for the same number of bands. Clearly, for well-localized WFs the storage requirements within the WF representation will be considerably reduced relative to the requirements within the Bloch function representation.

The above WF representation of the ideal PhC's GF allows us to determine physical quantities such as the density of states (DOS), $N(\omega)$, and the local density of states (LDOS), $N(\vec{r}, \omega)$. The latter is particularly useful when describing the radiation dynamics of active materials embedded in PhCs [54]. Within the WF representation, we obtain for the 2D LDOS of the ideal PhC

$$N(\vec{r}, \omega) = -\frac{2\omega}{\pi c^2} \epsilon_{\mathrm{per}}(\vec{r}) \sum_{\alpha,\beta} W^*_\alpha(\vec{r})\, G_{\alpha\beta}(\omega)\, W_\beta(\vec{r}). \tag{20}$$

Based on this we find a relatively simple expression for the 2D DOS of the ideal PhC within the WF representation

$$\begin{aligned} N(\omega) &= \frac{1}{V}\int_V \mathrm{d}^2 r \, N(\vec{r}, \omega) = -\frac{2\omega}{\pi c^2}\frac{1}{V}\int_V \mathrm{d}^2 r \, G(\vec{r}, \vec{r}; \omega) \\ &= -\frac{2\omega}{\pi c^2}\frac{1}{V_{\mathrm{wsc}}} \sum_n G_{n\vec{0};\, n\vec{0}}(\omega), \end{aligned} \tag{21}$$

where the integration is over the entire space, V_{wsc} denotes the volume of the Wigner–Seitz cell, and the orthonormality properties of the WFs, Equation (3), have been utilized.

In Figure 13, we display the WF-based results for the DOS (solid line) for E-polarized radiation in our model 2D PhC that consists of a square lattice of silicon posts ($r/a = 0.18$, $\epsilon_{\mathrm{Si}} = 12$). In the long wavelength limit, we observe the linear behavior that is characteristic for an effectively homogeneous 2D system (cf. the dashed line; also, see the appendix of [55] for details on the determination of the effective dielectric constant). For higher frequencies, we obtain (logarithmic) van-Hove singularities and step discontinuities at band edges that are characteristic for the DOS of 2D PhCs [56]. Finally, in Figure 14 we display the LDOS for several frequencies above and below the first band gap along one of the crystallographic axes and for a line through the unit cell that passes through the centre of a silicon post. For frequencies below the first band gap, we observe the characteristic concentration of the modes of this so-called 'dielectric band'

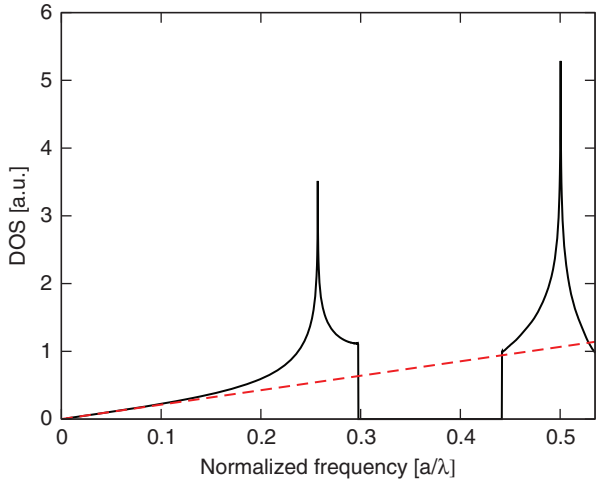

Figure 13. 2D DOS (solid line) for E-polarized radiation in a square lattice of silicon posts. The corresponding band structure of this model PhC is depicted in Figure 4(*a*). The DOS has been computed using the WF representation of the PhC's Green's function. The dashed line represents the corresponding linearly increasing 2D DOS for a homogeneous medium with a dielectric constant equal to the effective long-wavelength dielectric constant of the PhC. (The color version of this figure is included in the online version of the journal.)

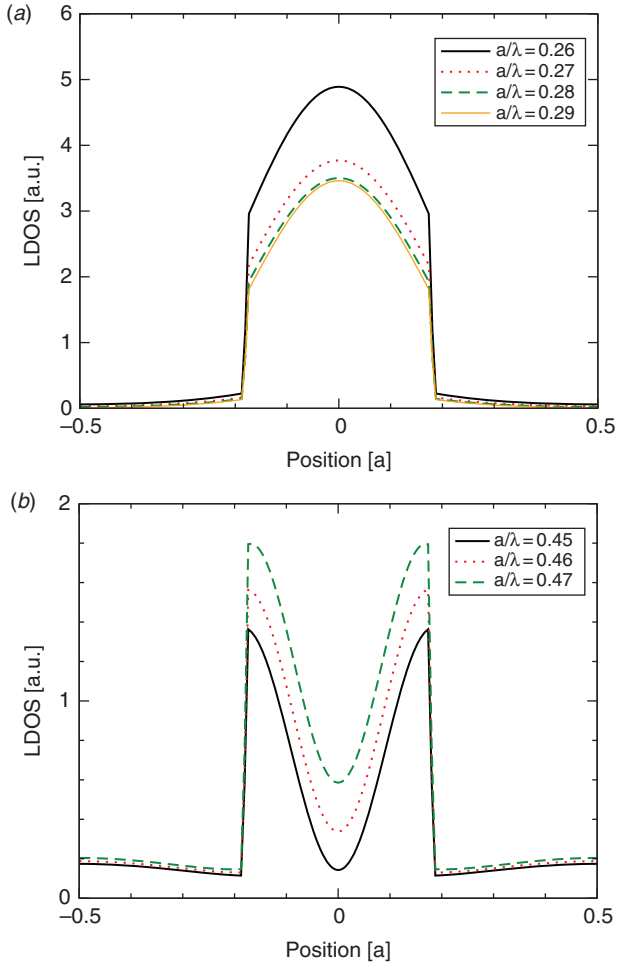

Figure 14. LDOS for E-polarized radiation in a square lattice of silicon posts for frequencies below (*a*) and above (*b*) the first photonic band gap. The corresponding band structure of this model PhC is depicted in Figure 4(*a*). The LDOS has been computed using the WF representation of the PhC's Green's function and is shown along a line through the unit cell that is parallel to the *x*-axis and passes through the centre of a silicon post. (The color version of this figure is included in the online version of the journal.)

within the high-dielectric-constant posts [3]. Similarly, for frequencies above the first band gap, we find the characteristic behavior of modes that belong to a so-called 'air band' (note the different scales of Figure 14(*a*) and (*b*)).

The availability of the GF for ideal PhC structures represents an excellent starting point for the analysis of disordered systems by adopting the well-trodden paths of electronic structure theory [53] to the case of PhCs. Moreover, it is tempting to speculate whether more sophisticated methods for full-fledged transport calculations such as the two-particle locator theory [57,58] can be adapted to the WF representation in order eventually to deliver quantitative statements about transport quantities, such as diffusion coefficients and localization lengths.

The above examples regarding 3D WFs and WF-based GF techniques for PhCs represent but a few of the ongoing developments and exciting future directions that this line of research may take. Additional and no less exciting avenues could be the development of a WF approach for membrane-type PhCs, where one could carry out full 3D computations with not much more than 2D effort – provided one finds an efficient way of dealing with out-of-plane scattering processes, i.e. the construction of guided and radiation modes within a WF representation and a treatment of their mutual coupling. Similarly, all the developments that we have presented in this review, have been worked out for linear systems and time-harmonic fields. A time-domain version of the WF approach would make an interesting addition to the rather limited number of efficient tools for time-domain computations.

Acknowledgements

The authors acknowledge the support of the Deutsche Forschungsgemeinschaft (DFG) and the State of Baden-Württemberg through the DFG-Center for Functional Nanostructures (CFN) within subproject A1.1. The Ph.D. student education of C.W. is embedded in the Karlsruhe

School of Optics & Photonics (KSOP). Some of the computations have been performed on the HP XC4000 at the Steinbuch Centre for Computing (SCC), Karlsruhe under the project NOTAMAX.

References

[1] Yablonovitch, E. *Phys. Rev. Lett.* **1987,** *58,* 2059–2062.
[2] John, E. *Phys. Rev. Lett.* **1987,** *58,* 2486–2489.
[3] Busch, K.; von Freymann, G.; Linden, S.; Mingaleev, S.F.; Tkeshelashvili, L.; Wegener, M. *Phys. Rep.* **2007,** *444,* 101–202.
[4] von Freymann, G.; Ledermann, A.; Thiel, M.; Staude, I.; Essig, S.; Busch, K.; Wegener, M. *Adv. Funct. Mater.* **2010,** *20,* 1038–1052.
[5] Baba, T. *Nature Photon.* **2008,** *2,* 465–473.
[6] Mortensen, N.A.; Xiao, S.; Pedersen, J. *Microfluid. Nanofluid.* **2007,** *4,* 117–127.
[7] Leung, K.M. *J. Opt. Soc. Am. B* **1993,** *10,* 303–306.
[8] Albert, J.P.; Jouanin, C.; Cassagne, D.; Bertho, D. *Phys. Rev. B* **2000,** *61,* 4381–4384.
[9] Albert, J.P.; Jouanin, C.; Cassagne, D.; Monge, D. *Opt. Quantum Electron.* **2002,** *34,* 251–263.
[10] Marzari, N.; Vanderbilt, D. *Phys. Rev. B* **1997,** *56,* 12847–12865.
[11] Busch, K.; Mingaleev, S.F.; Garcia-Martin, A.; Schillinger, M.; Hermann, D. *J. Phys.: Condens. Matter* **2003,** *15,* R1233–R1256.
[12] Whittaker, D.M.; Croucher, M.P. *Phys. Rev. B* **2003,** *67,* 085204.
[13] Sotirelis, P.; Albrecht, J.D. *Phys. Rev. B* **2007,** *76,* 075123.
[14] Mingaleev, S.F.; Schillinger, M.; Hermann, D.; Busch, K. *Opt. Lett.* **2004,** *28,* 2858–2860.
[15] Jiao, Y.; Mingaleev, S.F.; Schillinger, M.; Miller, D.A.B.; Fan, S.; Busch, K. *IEEE Photon. Technol. Lett.* **2005,** *17,* 1875–1877.
[16] Jiao, Y.; Fan, S.; Miller, D.A.B. *Opt. Lett.* **2005,** *30,* 141–143.
[17] Jiao, Y.; Fan, S.; Miller, D.A.B. *Opt. Lett.* **2005,** *30,* 302–304.
[18] Takeda, H.; Chutinan, A.; John, S. *Phys. Rev. B* **2006,** *74,* 195116.
[19] Hermann, D.; Schillinger, M.; Mingaleev, S.F.; Busch, K. *J. Opt. Soc. Am. B* **2008,** *25,* 202–209.
[20] Yeh, P. *Optical Waves in Layered Media*, 2nd ed.; John Wiley & Sons: Hoboken, NJ, 2005.
[21] Muradoglu, M.S.; Baghai-Wadji, A.R.; Ng, T.W. *J. Opt. Soc. Am. B* **2010,** *27,* 757–765.
[22] Des Cloizeaux, J. *Phys. Rev.* **1963,** *129,* 554–566.
[23] He, L.; Vanderbilt, D. *Phys. Rev. Lett.* **2001,** *86,* 5341–5344.
[24] Lidorikis, E.; Busch, K.; Li, Q.; Chan, C.T.; Soukoulis, C. *Phys. Rev. B* **1997,** *56,* 15090–15099.
[25] Johnson, S.G.; Joannopoulos, J.D. *Opt. Express* **2001,** *8,* 173–190.
[26] Schenk, O.; Gärtner, K. *Future Generation Comp. Sys.* **2004,** *3,* 475–487; Schenk, O.; Gärtner, K. *Elec. Trans. Numer. Anal.* **2006,** *23,* 158–179.
[27] Hermann, D.; Diem, M.; Mingaleev, S.F.; Garcia-Martin, M.; Wölfle, P.; Busch, K. *Phys. Rev. B* **2008,** *77,* 035112.
[28] Souza, I.; Marzari, N.; Vanderbilt, D. *Phys. Rev. B* **2001,** *65,* 035109.
[29] Des Cloizeaux, J. *Phys. Rev.* **1964,** *135,* A685.
[30] Des Cloizeaux, J. *Phys. Rev.* **1964,** *135,* A698.
[31] Krüger, E. *Phys. Stat. Sol. (b)* **1972,** *52,* 215–230.
[32] Krüger, E. *Phys. Stat. Sol. (b)* **1972,** *52,* 519–531.
[33] International Union of Crystallography. *International Tables for Crystallography*; Wiley-VCH: Weinheim, 2010.
[34] Sakoda, K. *Optical Properties of Photonic Crystals*; Springer Series in Optical Sciences, Vol. 80; Springer: Berlin, 2001.
[35] Monkhorst, H.; Pack, J. *Phys. Rev. B* **1976,** *13,* 5188–5192.
[36] Ye, Z.; Hu, X.; Li, M.; Ho, K.-M.; Cao, J.; Miyawaki, M. *Phys. Rev. B* **2009,** *80,* 035111.
[37] Busch, K.; John, S. *Phys. Rev. Lett.* **1999,** *83,* 967–970.
[38] Takeda, H.; Yoshino, K. *Phys. Rev. B* **2003,** *67,* 073106.
[39] Intonti, F.; Vignolini, S.; Türck, V.; Colocci, M.; Bettoti, P.; Pavesi, L.; Schweizer, S.L.; Wehrspohn, R.B.; Wiersma, D.S. *Appl. Phys. Lett.* **2006,** *89,* 211117.
[40] El-Kallassi, P.; Balog, S.; Houdre, R.; Baelt, L.; Li, L.; Francardi, M.; Gerardino, A.; Fiore, A.; Ferrini, R.; Zuppiroli, L. *J. Opt. Soc. Am. B* **2008,** *25,* 1562–1567.
[41] Vignolini, S.; Riboli, F.; Intonti, F.; Belotti, M.; Gurioli, M.; Chen, Y.; Colocci, M.; Andreani, L.C.; Wiersma, D.S. *Phys. Rev. E* **2008,** *78,* 045603(R).
[42] Kicken, H.H.J.E.; Alkemade, P.F.A.; van der Heijden, R.W.; Karouta, F.; Nötzel, R.; van der Drift, E.; Salemink, H.W.M. *Opt. Express* **2009,** *17,* 22005–22011.
[43] Nolte, P.W.; Pergande, D.; Schweizer, S.L.; Geuss, M.; Salzer, M.; Makowski, B.T.; Steinhart, M.; Wehrspohn, R.B.; Weder, C. *Proc. SPIE* **2009,** *7393,* 73930S.
[44] Intonti, F.; Vignolini, F.; Riboli, F.; Zani, M.; Wiersma, D.S.; Balet, L.; Li, L.H.; Francardi, A.; Gerardino, A.; Fiore, A.; Gurioli, M. *Appl. Phys. Lett.* **2009,** *95,* 173112.
[45] Vignolini, S.; Riboli, F.; Wiersma, D.S.; Balet, L.; Li, L.H.; Francardi, M.; Gerardino, A.; Fiore, A.; Gurioli, M.; Intonti, F. *Appl. Phys. Lett.* **2010,** *96,* 141114.
[46] Nolte, P.W.; Pergande, D.; Schweizer, S.L.; Geuss, M.; Salzer, M.; Makowski, B.T.; Steinhart, M.; Mack, P.; Hermann, D.; Busch, L.; Weder, C.; Wehrspohn, R.B. Photonic Crystal Devices with Multiple Dyes by Consecutive Local Infiltration of Single Pores. *Adv. Mater.* [Online early access]. DOI: 10.1002/adma.201001718. Published Online: Aug 23, 2010.
[47] Vignolini, S.; Riboli, F.; Intonti, F.; Wiersma, D.S.; Balet, L.; Li, L.H.; Francardi, M.; Gerardino, A.; Fiore, A.; Gurioli, M. *Appl. Phys. Lett.* **2010,** *97,* 063101.
[48] Mingaleev, S.F.; Busch, K. *Opt. Lett.* **2003,** *28,* 619–621.
[49] Staude, I.; Thiel, M.; Essig, S.; Wolff, C.; Busch, K.; von Freymann, G.; Wegener, M. *Opt. Lett.* **2010,** *35,* 1094–1096.
[50] Sipe, J. *Phys. Rev. E* **2000,** *62,* 5672–5677.

[51] Fallert, J.; Roman, Dietz, R.J.B.; Sartor, J.; Schneider, D.; Klingshirn, C.; Kalt, H. *Nature Photon*. **2009,** *3,* 279–282.
[52] Patterson, M.; Hughes, S.; Schulz, S.; Beggs, D.M.; White, T.P.; O'Faolain, L.; Krauss, T.F. *Phys. Rev. B* **2009,** *80,* 195305.
[53] Gonis, A. *Green Functions for Ordered and Disordered Systems*; North-Holland: Amsterdam, 1992.
[54] Vats, N.; John, S.; Busch, K. *Phys. Rev. A* **2002,** *65,* 043808.
[55] Kirchner, A.; Busch, K.; Soukoulis, C. *Phys. Rev. B* **1998,** *57,* 277–288.
[56] Busch, K.; John, S. *Phys. Rev. E* **1998,** *58,* 3896–3908.
[57] Kopp, T. *J. Phys. C: Solid State Phys*. **1984,** *17,* 1897.
[58] Kopp, T. *J. Phys. C: Solid State Phys*. **1984,** *17,* 1919.